Microstructural evolution and its impact on the mechanical strength of typical alkali-activated slag subjected to accelerated carbonation

Thi Nhan Nguyen, Quoc Tri Phung, Lander Frederickx, Diederik Jacques, Alexandre Dauzères, Jan Elsen, Yiannis Pontikes

Developments in the Built Environment 19 (2024) 100519

Contents lists available at ScienceDirect

Developments in the Built Environment

journal homepage: www.sciencedirect.com/journal/developments-in-the-built-environment

Microstructural evolution and its impact on the mechanical strength of typical alkali-activated slag subjected to accelerated carbonation

Thi Nhan Nguyen [a,d,*], Quoc Tri Phung [a,**], Lander Frederickx [a], Diederik Jacques [a], Alexandre Dauzeres [b], Jan Elsen [c], Yiannis Pontikes [d]

[a] Institute for Environment, Health, and Safety, Belgian Nuclear Research Centre (SCK CEN), 2400, Mol, Belgium
[b] Institute of Radiation Protection and Nuclear Safety (IRSN), PSE-ENV/SEDRE/LETIS, 92260, Fontenay-aux-Roses, France
[c] Department of Earth and Environmental Sciences, KU Leuven, 3001, Leuven, Belgium
[d] Department of Materials Engineering, KU Leuven, 3001, Leuven, Belgium

ARTICLE INFO

Keywords:
Alkali-activated slag
Accelerated carbonation
Water content
Microstructure
Mechanical strength

ABSTRACT

This study aims to comprehensively investigate the evolution of microstructure, mechanical strength, and their correlation in alkali-activated slag (AAS) mortars, designed for application in the immobilization of liquid radioactive waste, under accelerated carbonation conditions (1% CO_2, 20 °C and 60% RH). To gain insights into the underlying microstructural changes, CO_2 uptake and decalcification of C-A-S-H were analyzed using TGA/DSC and EDS. The pore structure of AASs was systematically assessed across nano- to macro-scales, employing N_2-adsorption, MIP, and SEM segmentation. Generally, carbonation led to a decrease in total porosity, primarily attributed to the reduction in meso-macropore volume. However, the pore size distribution of AAS exhibited a complex alteration over varying carbonation durations. Carbonation significantly reduced flexural strength, whereas its effect on compressive strength was comparatively milder. Notably, an evident linear correlation emerged between porosity and compressive strength in both reference and carbonated AASs.

1. Introduction

Alkali-activated materials (AAMs) have emerged as environmentally friendly alternative binders to ordinary Portland cement (OPC) in the past decades because of their ability to reuse industrial byproducts and lower CO_2 production emissions (Provis et al., 2015; Puertas et al., 2018; Hertel and Pontikes, 2020). Among AAMs, alkali-activated slag (AAS) produced from ground granulated blast furnace slag (GGBFS) has garnered significant interest due to its outstanding performance, such as excellent mechanical properties and outstanding durability in various aggressive environments (Lecomte et al., 2006). Specially, AAMs in general and AASs in particular have recently been found as promising hosting matrices for liquid radioactive waste immobilization (Cantarel et al., 2015, 2018; Reeb et al., 2022, 2023). However, AASs are potentially altered or degraded during exposure to diverse environments, depending on their application fields. Therefore, understanding changes in the AASs under typical conditions is crucial for designing suitable materials for each application. Carbonation is one of the main degradation processes of AAS as its structures are expected to work under atmospheric carbonation (0.04% CO_2). Even in radioactive waste disposal, waste-form drums or monoliths disposed in (near)-surface repository may also be attacked by atmospheric CO_2. Although numerous studies have been performed to investigate the carbonation resistance of AAS, considering the influence of the slag content (Bernal et al., 2011; Nedeljković et al., 2019), types and concentration of activators (Ben Haha et al., 2011; Puertas and Torres-Carrasco, 2014), CO_2 concentration (McCaslin and White, 2021), exposure duration (Ye and Radlińska, 2017; Yamazaki et al., 2021), and humidity (Xu et al., 2022), the evolution of AASs with respect to water-to-binder ratio still remains a topic of active research. In particular, there is no research on the carbonation of typical AASs designed for liquid wasteimmobilization.

Carbonation induces a decrease in pore solution alkalinity and then leads to the decalcification of Ca-bearing phases, notably affecting primary tetrahedral aluminosilicate C-(A)-S-H phase alongside secondary phases (e.g., Mg,Al-layer double hydroxides) (Shi et al., 2018; Bernal et al., 2014a; Puertas et al., 2006). This processes exhibit variation

* Corresponding author.
** Corresponding author.
E-mail addresses: thinhan.nguyen@kuleuven.be (T.N. Nguyen), quoc.tri.phung@sckcen.be (Q.T. Phung).

https://doi.org/10.1016/j.dibe.2024.100519
Received 26 January 2024; Received in revised form 21 June 2024; Accepted 6 August 2024
Available online 12 August 2024

Table 1
Oxide composition (wt. %) of GGBFS.

Oxides	SiO_2	Al_2O_3	Fe_2O_3	CaO	MgO	K_2O	Na_2O	TiO_2	SO_3	LOI
GGBFS	32.4	11.1	0.60	43.40	7.77	0.53	0.27	1.01	2.41	0.51

across different AASs, depending on the complexity of solid-phase assemblages and chemical composition of the pore solution of the materials. Compared to OPC, AAS has been reported to be more vulnerable to accelerated carbonation (Puertas et al., 2006; Bakharev et al., 2001a). This was explained by the absence of portlandite (CH) in AAS, which typically serves as a buffering phase, consequently delaying the decalcification of the main phase (C-S-H gel) in OPC. In contrast, the presence of dissolved CO_2 in the pore solution of AAS changes the solution equilibria, facilitating the creation of carbonate products (e.g., sodium and calcium (bi)carbonates). Consequently, the decalcification of the C-A-S-H gel happens to release Ca^{2+}, thereby compensating for the deficiency of cations in the pore solution (Bernal, 2015). Two stages of carbonation process of AAS have been proposed (Nedeljković et al., 2019; Bernal et al., 2012; Nguyen et al., 2022) as follows: (i) diffusion of CO_2 and carbonation in the pore solution, leading to a pH reduction and formation of Na-rich carbonate products; (ii) decalcification of C-A-S-H gel and other Ca-contained secondary phases to form $CaCO_3$ precipitates.

So far, research on the carbonation of AAS has mainly focused on mineralogical alteration of the material (Shi et al., 2018; Bernal et al., 2014a, 2015a; Nedeljković et al., 2018a). Knowledge on the influence of carbonation on AAS's microstructure, particularly concerning large pore scales, still remains uncertain. Carbonation usually refines the pore structure of OPC owing to the precipitation of calcite (Chen et al., 2006; Phung, 2015a), referred as carbonation shrinkage. This phenomenon in AAS is expected to be less extent due to the lack of portlandite and the considerably lower Ca/Si ratio of C-A-S-H compared to C-S-H in OPC, leading to less crystalline $CaCO_3$ products formed and filled in pore space. However, due to the finer pore structure of AAS compared to OPC at the same w/b ratio (Ye et al., 2017), the formation of crystalline carbonation products in AAS may induce higher crystallization stress, potentially resulting in cracking in the matrix. Thus, changes in the microstructure of AAS under carbonation are not only associated with mineralogical evolution but also with the initial pore characteristics of the material. Furthermore, decalcification of C-A-S-H might result in a loss of cohesion within this gel, further contributing to the formation of cracks. Indeed, Ye et al. (Ye and Radlińska, 2017) reported the formation of micro-cracks in AAS paste, and cracking occurrence was also indicated by Shi et al. (Shi et al.) upon carbonation. Despite the insignificant effect on the geochemical properties of AAS (longer than 28 days of curing) (Nguyen et al., 2022; Zhang et al., 2021), water-to-binder (w/b) ratio significantly influences its pore structure and transport properties, as evidenced by a more porous structure (Bernal et al., 2015b; Li et al., 2017) and a significant increase in the water permeability of the material when increasing w/b ratio (Nguyen et al., 2021) from 0.35 to 0.55. Consequently, w/b ratio can affect the CO_2 diffusion into the AAS matrix and the subsequent kinetics of carbonation reactions. Therefore, w/b ratio is expected to affect the carbonation resistance of AAS. However, little attention has been paid to the impact of the w/b ratio on the microstructural properties of AAS during carbonation.

As a consequence of the microstructural changes in AAS upon carbonation, its physical properties (e.g., mechanical strength) are potentially altered. Observations on the influence of silicate modulus (SiO_2/Na_2O) (Li et al., 2017; Song et al., 2014), activator dose (Bernal, 2015), carbonation duration (Puertas et al., 2006; Mei et al., 2021), and composition of precursors (Lee et al., 2017) on the compressive strength of AAS upon carbonation were reported. Puertas et al. (2006) indicated a decline of up to 14% in the compressive strength of water glass-activated slag after four-month carbonation and no further reduction after eight-month exposure. Also, Song et al. (2014) noted a loss in the compressive strength of AAS due to the formation of low-cohesive silica gels in the carbonated matrix. This reduction was attributed to microcrack formation and weakened matrix due to the decalcification of the C-A-S-H gel. However, a strength loss (Li et al., 2017; Song et al., 2014; Mei et al., 2021; Lee et al., 2017) has not always been reported; a stable (Bernal, 2015) or even increased (Puertas et al., 2006; Bernal, 2015) compressive strength of AAS after carbonation has also been documented, which leads to a controversial debate on the changes in the compressive strength of AAS due to carbonation. One of the main parameters affecting the changes in compressive strength upon carbonation was the alkaline activator, in which NaOH-activated slag showed an increase in its compressive strength, whereas a decreased or maintained strength was observed for Na-silicate-activated slag after carbonation (Mei et al., 2021; Lee et al., 2017). From current reports, it appears that alteration in compressive strength is defined by the coupled effect between the cohesion loss of C-A-S-H gel due to its decalcification and the formation of $CaCO_3$ crystals during carbonation. The former causes a strength loss, while the latter strengthens the AAS material. NaOH-activated slag exhibits a higher Ca/Si ratio and shorter silicate chain length compared to Na-silicate activated slag, and thereby tends to promote the formation of $CaCO_3$ products to refine the structure and ultimately enhances its compressive strength (Puertas et al., 2006). Furthermore, a higher hydrotalcite content in NaOH-activated slag than in Na-silicate activated slag (Bernal et al., 2014b) also contributes to improve the carbonation resistance of the material. This phase has a capability to absorb a considerable amount of CO_2 that diffuses into the matrix, effectively eliminating the decalcification of C-A-S-H gel. Notably, similar to the case of microstructure, the impact of w/b ratio on the mechanical strength of AAS under carbonation remains inadequately documented.

It is evident from the overview above that, despite numerous studies on the carbonation of AASs, the alteration in the microstructure and mechanical properties of AASs is not fully understood and even controversial. Therefore, the main objective of the study is to deeply investigate changes in the pore structure covering from nano to macro scales and mechanical strength of AAS under accelerated carbonation (1% CO_2, 20 °C and 60% relative humidity). Importantly, this study was done on typical AASs, which were designed for application in liquid radioactive waste immobilization. Furthermore, the important role of w/b ratio in the complex evolution in the microstructure and mechanical strength of AAS is highlighted. The microstructural properties of the AASs before and after carbonation were characterized by multiple techniques, including nitrogen adsorption (N_2-adsoption), mercury intrusion porosimetry (MIP), and scanning electron microscopy (SEM). Thermogravimetric analysis (TGA) and energy-dispersive X-ray spectroscopy (EDS) were used to clarify the underlying reasons of microstructural changes. This work is the first stage in the development of a suitable AAS matrix for radioactive liquid waste immobilization, of which carbonation resistance is one of the important assessment criteria.

2. Materials and test setup

2.1. Materials and mixing procedure

GGBFS, with the chemical compositions reported in Table 1, was supplied by Ecocem Benelux. The activating solution was produced from solid NaOH pellets (99% purity, VWR Chemicals), sodium silicate solution from VWR Chemicals (consisting of 8.97% Na_2O, 26.78% SiO_2, 64.25% H_2O), and additional water. First, the NaOH pellets were dissolved in distilled water to obtain a 5M solution. Subsequently, sodium

Table 2
Formulation of AAS mortars (mole ratios).

Mortars	w/b[a]	SiO_2/Al_2O_3	SiO_2/Na_2O	H_2O/Na_2O	Ms[b]
AAS 0.35	0.35	5.23	8.79	32.02	0.45
AAS 0.45	0.45	5.23	8.79	41.17	0.45
AAS 0.55	0.55	5.23	8.79	50.32	0.45

[a] Water in w/b ratio includes water content in the activating solution. The SiO_2 and Na_2O were accounted for both GGBFS and the activators.
[b] Silicate modulus (Ms: SiO_2/Na_2O) of the activating solution.

silicate was gradually poured into the NaOH solution and stirred until obtaining a homogeneous solution. Extra water was added to this solution obtain the targeted w/b ratios of 0.35, 0.45, and 0.55. The activating solutions were allowed to equilibrate for approximately 24 h prior use. The activator dosage was 4.0 wt% NaOH (4 g NaOH/100 g GGBFS) (Nguyen et al., 2022). River sand with a particle size smaller than 2 mm and a density of 2.67 g/cm^3 was used as fine aggregate. It is important to note that the volume fraction of the aggregate utilized in this study was fixed at 20 vol% (approximately 26 wt%) relative to the total volume of the mortar, which is relevant to the use of AAS for liquid waste immobilization context (expectation of maximizing waste loaded in AAS matrix) (Nguyen et al., 2022; Predis). The formulations of AASs are listed in Table 2.

GGBFS and the activating solution were mixed together for 2 min in a bowl, using a rotary mixer at low speed. Subsequently, sand was poured into the mixture and mixed for 2 min at low speed. The mixing was stopped to scrape everything from the bowl's wall and then mixed for 2 min at high speed. The mortar slurry was then cast into prism moulds (40 × 40 × 160 mm) and cured at room temperature under sealed conditions for 24 h. Afterwards, samples were demoulded and cured at 20 °C for 27 days in a curing cabinet controlled the relative humidity (RH) at 95% ± 2.

2.2. Accelerated carbonation process

After curing, the sample prisms were preconditioned at 20 °C and 60% RH until the difference between two weighing measurements in at least 24h of a sample was less than 0.2%. Once the samples were preconditioned, six samples of each w/b ratio were placed in a climate chamber for accelerated carbonation testing. The carbonation conditions were set at 20 °C, 60% RH, and 1% CO_2, which followed the EN standard 13295 (Standardization, 2004). After 7, 14, and 28 days of carbonation, the carbonation depth and mechanical strength of the samples were measured. As a reference, the carbonation depth and mechanical strength tests were also done for samples before carbonation (at 28 days of curing). The carbonation setup is shown in Fig. 1. The 3 mm-depth fractions (from the reactive surface) of the carbonated and reference samples were subjected to characterization. Such depth was selected to maximize the carbonation impact so that changes of the samples induced by carbonation can be clearly observed. Moreover, that can allow the results among different samples being comparable.

3. Sample testing and characterization

3.1. Determination of mechanical strengths and carbonation depth

For each sample, mechanical strengths were determined using a hydraulic press (Matest, Italy) with a capacity of 250 kN for compressive strength and 15 kN for flexural strength. First, the flexural strengths of the samples were determined at a loading rate of 0.05 kN/s. Then, carbonation depth was measured by spraying 0.5 wt% phenolphthalein (in ethanol) on the fresh surface of the half prisms obtained after the flexural strength test. After approximately 30 min of spraying, carbonation depths were determined at multiple points from four sides of the surface (five measurement points on each side), and the average value of the 20 measurements was reported as the carbonation depth of the sample (Vogler et al., 2020; Choi et al., 2017). Subsequently, compressive strength measurements at a loading rate of 2.4 kN/s were performed on these half prisms using the same device (Standard, 2009). The average of two measurements of the flexural strength and four measurements of the compressive strength were reported for each sample.

3.2. Thermogravimetric analysis

The samples within 3 mm from the exposed surface was cut and freeze-dried. The dried samples were then ground under the N_2-supplied environment. TG analyses were performed on approximately 40 mg of the dried powder sample using a Netzsch STA 409 PC instrument. The temperature was increased from room temperature to 1000 °C at a heating rate of 10 °C per min under a constant 50 ml/min argon flow.

3.3. N_2-adsorption

Nitrogen physisorption analyses (Frederickx et al., 2022) were performed to determine the specific surface area and quantify the pore sizes in the range of 2–45 nm. Freeze-dried samples sieved between 500 and 800 μm were measured using a TriStar 3020 device at 77 K. The specific surface area was calculated using the Brunauer–Emmett–Teller (BET) method applied to the adsorption isotherm. The pore size distribution was calculated by using the Barret-Joyner-Halenda (BJH) method

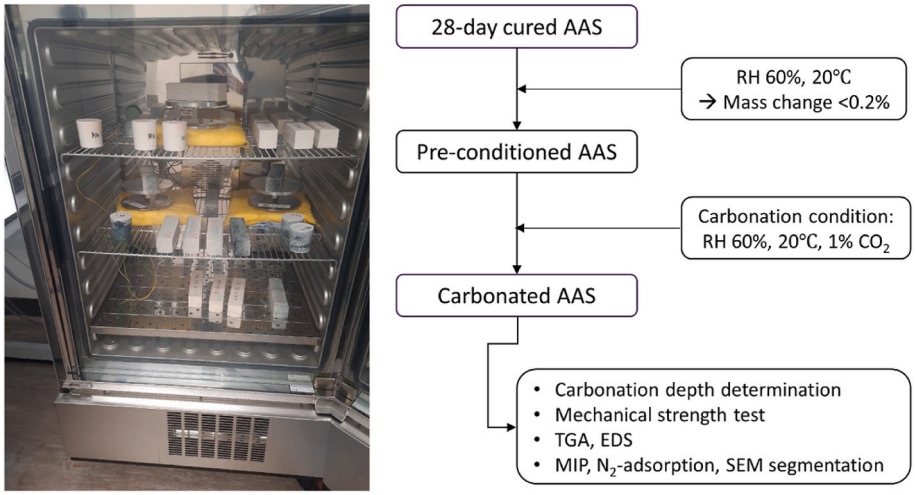

Fig. 1. Carbonation test setup for AAS mortars.

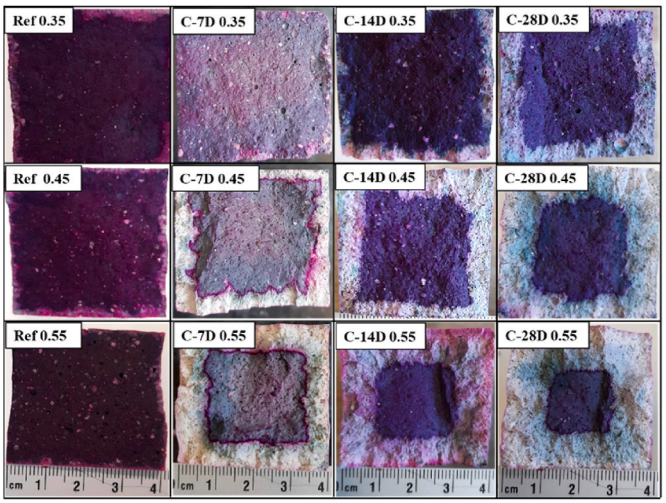

Fig. 2. Cross-sections of the reference (Ref) and carbonated samples (7-day carbonation: C-7D, 14-day carbonation: C-14D, and 28-day carbonation: C-28D) after spraying phenolphthalein.

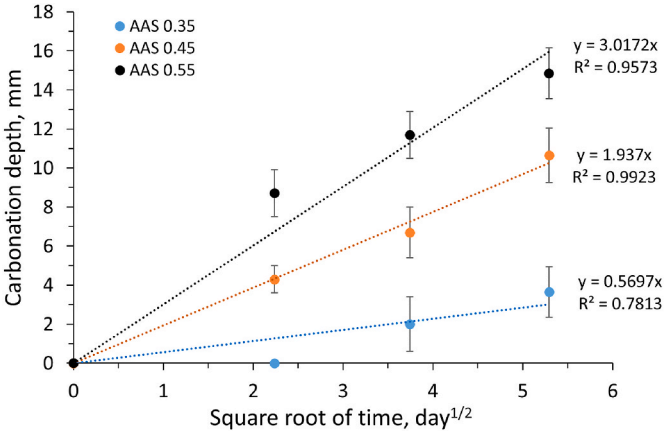

Fig. 3. Carbonation depth of samples with three w/b ratios over carbonation duration of 7, 14, and 28 days.

(Barrett et al., 1951) applied to the adsorption isotherm.

3.4. Mercury intrusion porosimetry

The porosity and pore size distribution in the range of 0.007–450 μm were measured by MIP, using an AutoPore IV 9500 device, with a maximum mercury pressure of 200 MPa. Samples with a grain size of approximately 3 mm were freeze-dried prior subjected to measurement. A contact angle of 140° was used to calculate the pore-size distribution using the Washburn equation.

3.4.1. Scanning electron microscopy

To understand the morphology of AASs and their pore structure at larger size range, SEM was applied. Specimens with a thickness of approximately 1 cm, perpendicular to the reactive surface, were used for SEM imaging. These specimens were embedded in an epoxy resin, polished using progressively finer sandpaper, and finally polished with diamond pastes ranging from 3 to 0.25 μm in diameter. The quality at each polishing step was monitored using an optical microscope. Backscattered electron images were recorded using a Phenom Desktop SEM at an accelerating voltage of 10 keV. Ten images per sample were obtained at a magnification of 1000 × for image segmentation and quantification of the micro-macro pore volume. Higher magnification images were also taken for detailed examination. EDS spot analyses targeting all the major phases were performed at a voltage of 15 keV with an analysis time of 40s per spot.

4. Results and discussion

4.1. Carbonation depth

Fig. 2 shows the carbonation depths of the AAS samples. The uncarbonated zone is depicted by the purple core, while the carbonated region (with a pH lower than ~9) is represented by the gray area (Phung, 2015b). Distinct carbonated zones were visually observed among samples, with greater depths noticeable in the samples under longer exposure and with higher w/b ratios. In particular, the linear relationship between the carbonation depth and the square root of time, shown in Fig. 3, implied that CO_2 diffusion was the dominant transport process in the AASs' carbonation (Phung, 2015b, 2015c; Phung et al., 2015a). The slopes of the fitted linear functions present their carbonation rates. Compared to the carbonation rate of cement at the same carbonation conditions, the AASs in this study exhibited a greater

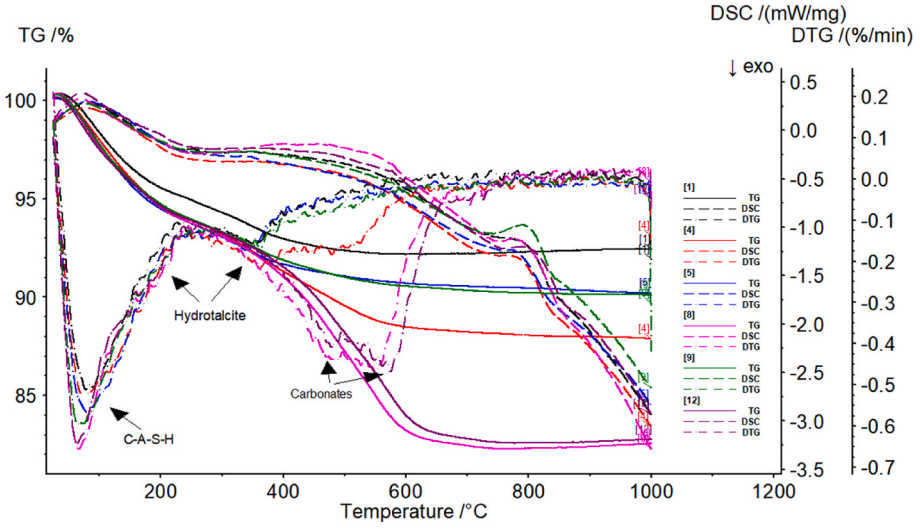

Fig. 4. TG, DTG and DSC curves of the AASs before (Ref) and after 28 days of carbonation (C-28D): Ref 0.35 (1), C-28D 0.35 (4), Ref 0.45 (5), C-28D 0.45 (8), Ref 0.55 (9), C-28D 0.55 (12).

Table 3
Mass loss of reference (Ref) and 28-day carbonated (C-28D) samples obtained by TGA.

Sample ID	Carbonate-containing phases (wt. %)					
	30–220 °C (C-A-S-H)	220–450 °C (hydrotalcite)	450–700 °C (carbonates)	Total mass loss	From TG	From XRD (vaterite) (Nguyen et al., 2022)
Ref 0.35	5.05	2.68	0.28	8.02	0.64	–
Ref 0.45	5.96	2.85	1.04	9.22	2.36	–
Ref 0.55	5.95	2.96	1.20	10.22	2.73	–
C-28D 0.35	5.79	3.05	3.09	12.28	7.02	1.20
C-28D 0.45	6.22	3.12	8.49	17.93	19.30	11.10
C-28D 0.55	5.92	3.50	7.96	17.41	18.09	13.40

carbonation rate than cements with the same w/b ratios, i.e., 0.57 mm/day$^{1/2}$ of AAS vs 0.03 mm/day$^{1/2}$ of cement at the w/b ratio of 0.35; and 1.94 mm/day$^{1/2}$ of AAS vs 0.79 mm/day$^{1/2}$ of cement at the w/b ratio of 0.45 (Shah and Bishnoi, 2018). These findings once again confirm the high susceptibility to carbonation of AAS materials at 1% CO_2. Also, faster carbonation rates of AASs than OPC were observed under other exposure conditions, i.e., 10–20% of CO_2, 70% RH (Bakharev et al., 2001b) and 5% of CO_2, 40 °C (Cadore et al., 2019). Specifically, the carbonation rate significantly increased (approximately fivefold) upon elevating the w/b ratio from 0.35 to 0.55, confirming the substantial impact of the w/b ratio on the carbonation resistance of the AASs. An increase in the w/b ratio corresponds to a higher porosity and larger pore size distribution (shown later in Section 4.3), promoting the CO_2 diffusion into the AAS matrix and consequently yielding a higher rate of carbonation.

4.2. CO_2 uptake and mineralogical changes due to carbonation

The TG and its derivative (DTG) curves of the reference (Ref) and the 28-day carbonated (C-28D) samples are shown in Fig. 4. Thermal decomposition spanning over a large temperature range was observed in the Ref samples, occurring from 30 °C to approximately 1000 °C, attributed to the sequential loss of water in different phases. The process can be divided in two stages: (i) the first stage spans from 30 to 220 °C, assigned to the mass loss resulting from the evaporation of free water from pore space and physically bound water within C-A-S-H network (Ruan et al., 2020); and (ii) the subsequent stage, ranging from 220 to approximately 450 °C, corresponds to the mass loss due to the dehydration of hydrotalcite-like layered double hydroxides (LDHs) (McCaslin and White, 2021; Abdalqader et al., 2019). At the temperature higher than 450 °C, minimal mass loss was observed in all Ref samples. A minor effect of the w/b ratio on the thermal resistance of AASs was presented, i.e., difference in the total mass loss was only 2.2 wt% when the w/b ratio increased from 0.35 to 0.55 (Table 3). Furthermore, the DTG peak intensities attributed to both the C-A-S-H gel and hydrotalcite-like LDHs in the Ref samples showed a notable similarity. The finding agrees with the quantitative XRD and ^{29}Si MAS NMR results for the phase assemblages of the AASs, reported in our previous study (Nguyen et al., 2022).

For 28-day carbonated samples (C-28D), the thermal decomposition encompassed a broader temperature range compared to that of the Ref samples. A remarkable mass loss was observed in the temperature range between 450 and 700 °C. It was assigned to the decarbonation of carbonate-contained phases such as magnesium carbonate (Ruan et al., 2020; Pavlík et al., 2016; Jin et al., 2014) and less crystalline $CaCO_3$ (e.g., vaterite and aragonite) (Shi et al., 2018; Yang et al., 2023; Ye et al., 2020), which was less stable than calcite decomposed at 700–800 °C (Pavlík et al., 2016). In this case, the mass loss within that temperature range was primarily assigned to vaterite, identified as the only carbonate phase detected by XRD measurements in the carbonated mortars (Nguyen et al., 2022). If considering that only vaterite decomposed between 450 and 700 °C, forming CaO and CO_2, the quantity of $CaCO_3$ (vaterite) can be calculated based on the mass loss (Table 3) and the molar masses as follows:

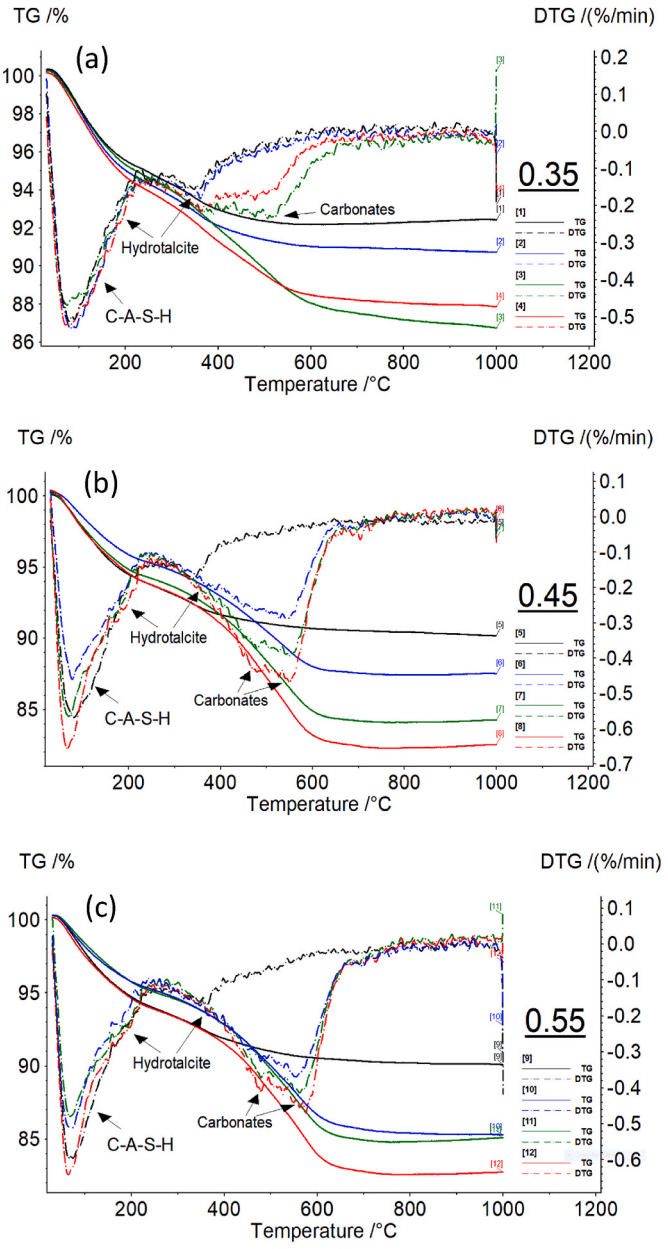

Fig. 5. The TG and DTG curves of the AASs with w/b ratios of 0.35 (a), 0.45 (b), and 0.55 (c) before and after carbonation: Ref (black), C-7D (blue), C-14D (green) and C-28D (red). (For interpretation of the references to color in this figure legend, the reader is referred to the Web version of this article.)

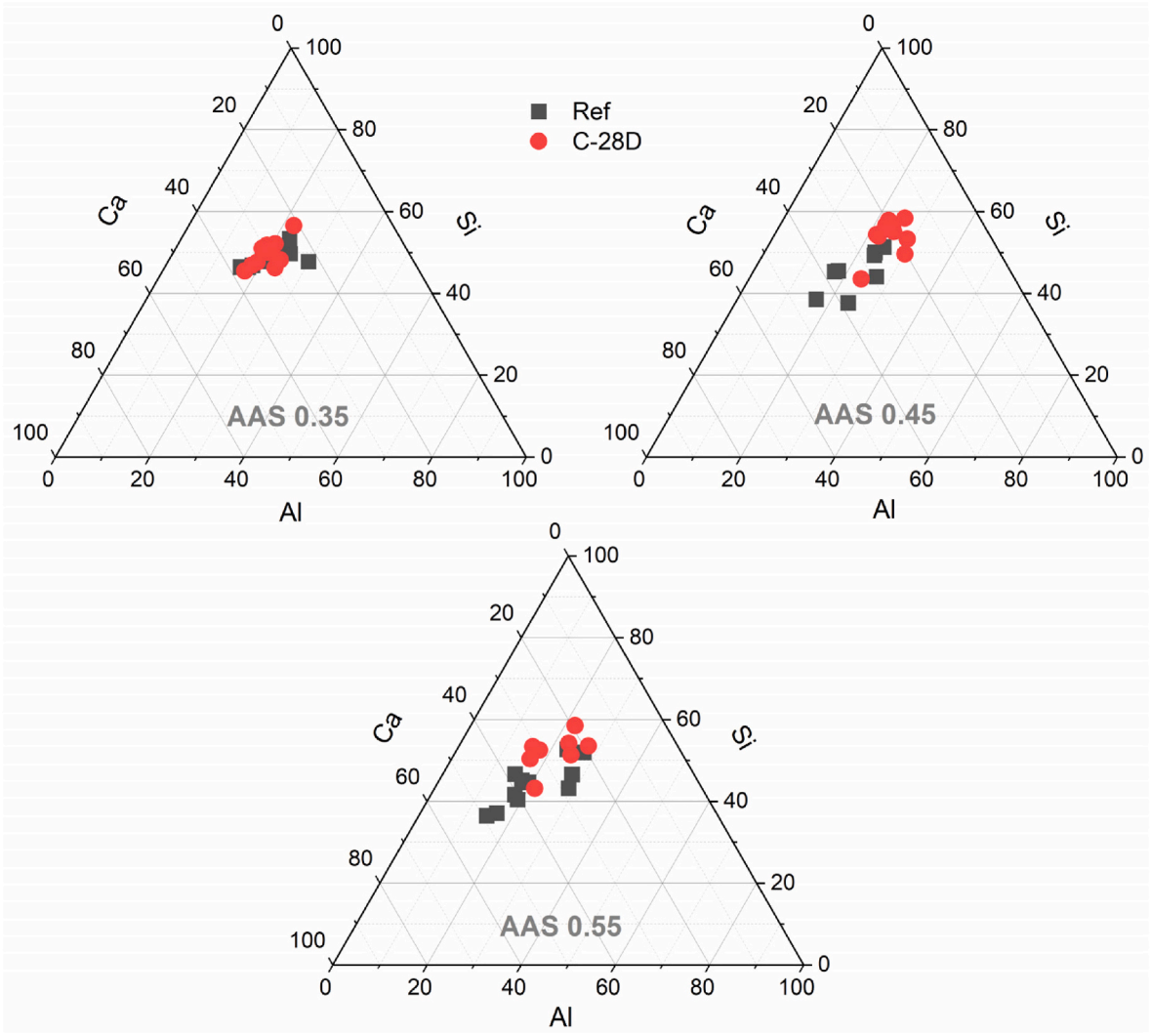

Fig. 6. Ternary diagrams of 3 major elements (Ca, Si, and Al) in C-A-S-H gel of the reference (Ref) and 28-day carbonated samples (C-28D), obtained by semi-quantitative SEM/EDS point analysis.

$$CaCO_{3,TG} = mass\ loss_{450-700\ ^\circ C} \times \frac{M_{CaCO_3}}{M_{CO_2}} \quad (1)$$

where M_{CaCO_3} and M_{CO_2} are 100 g/mol and 40 g/mol, respectively. The calculation was done for both the Ref and carbonated samples, and the obtained results were shown in Table 3. Interestingly, the Ref samples also exhibited a small amount of carbonate, suggesting a possible natural carbonation occurred during the samples preparation. The signals of carbonate in the reference samples were also identified by FTIR (Nguyen et al., 2022). Compared to the vaterite content quantified by XRD, the carbonate content determined from TG analysis appears notably higher (Table 3). This discrepancy is potentially due to the extensive formation of amorphous carbonate, which remains undetected by XRD analysis. Notably, the carbonated AASs with lower w/b ratios appeared to contain a higher proportion of amorphous carbonates, i.e., 82.9%, 42.5%, and 25.9% of total carbonate content in the carbonated samples C-28D 0.35, C-28D 0.45, and C-28D 0.55, respectively. The carbonated samples also revealed a slightly higher mass loss between 220 °C and 450 °C than the Ref ones, suggesting that CO_2 was adsorbed by hydrotalcite as also reported in (McCaslin and White, 2021; Sahoo et al., 2014). The CO_2 uptake in the samples then can be evaluated mainly based on the quantified carbonate content and the CO_2 absorbed by hydrotalcite (Table 3). It appears that the CO_2 uptake was approximately twice as high in the samples with the w/b ratios of 0.45 and 0.55 compared to the AAS 0.35, potentially attributed to the denser matrix of AAS 0.35 restraining the diffusion of CO_2 into the sample (Section 4.3). The mass loss of all samples increased with increasing the carbonation durations, shown in Fig. 5. The longer the carbonation duration, the more accelerated carbonation, even all these fractions belong to the carbonated zone (the cases of AAS 0.45 and AAS 0.55, Fig. 2).

Consistent with the TG analysis, the DSC results (Fig. 4) illustrate an endothermic peak centered at around 80 °C, representative to the dehydration of C-A-S-H gel (Ruan et al., 2020). This peak appears relatively sharper for the carbonated samples, suggesting a modification in water corporation within the gel network or a modified gel after carbonation. In addition, a broad endothermic peak, observed in the temperature range of 220–700 °C, was linked to the dehydration of hydrotalcite in the reference samples. In the C-28D samples, this peak presents to the overlapped processes of the dehydration and decarbonation of hydrotalcite and the decarbonation of carbonates. This explains for the higher intensity of the peak in the carbonated samples than in the Ref ones. Furthermore, another small endothermic peak was detected around 800 °C for all samples. This peak is related to the phase transformation of C-(A)-S-H to wollastonite ($CaSiO_3$) (Myers et al., 2015), in which only ~0.1H_2O/Si is released, rather than the decomposition of calcite.

To better understand the underlying changes in the gel chemical composition upon carbonation and to support the TG-DSC results, EDS

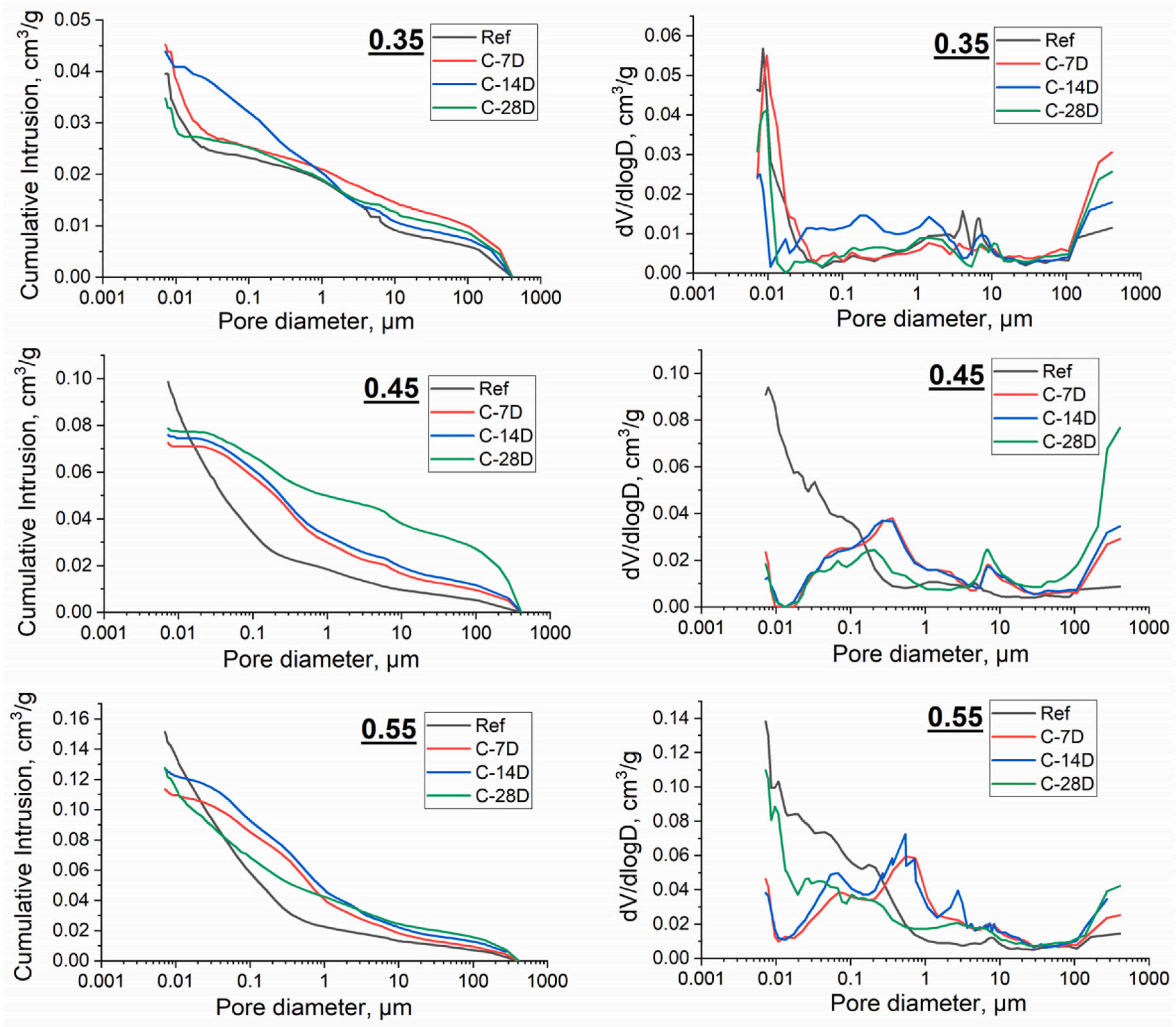

Fig. 7. Cumulative pore volume (left) and pore size distribution (right) of the AASs before (Ref) and after carbonation intervals (7 days: C-7D, 14 days: C-14D, 28 days: C-28D), assessed by MIP.

spot analyses, focusing on the C-A-S-H gel area of the Ref and C-28D samples, were carried out (Fig. 6). The Ca/Si ratio showed a small alteration after carbonation in the AAS 0.35 (e.g., a decrease of Ca/Si ratio from 0.59 to 0.57), suggesting a limited carbonation (or minimal decalcification) on this sample. This observation agrees with the small change in its DTG peak corresponding to the C-A-S-H gel (Fig. 5) and the smallest amount of carbonate products. However, the C-A-S-H gel of the samples with higher w/b ratios showed a more considerable Ca/Si reduction after carbonation, i.e., decreasing from 0.70 to 0.40 in AAS 0.45 and from 0.76 to 0.52 in AAS 0.55. The decreasing observation agrees well with the Ca/Si reduction indicated in other AAS materials after natural and accelerated carbonation (Yang et al., 2023; Bernal et al., 2013a, 2013b). Specifically, the Ca/Si value of Ref 0.45 in this study closely aligns with the Ca/Si ratio (0.6–0.7) observed in the AAS concrete with a w/b ratio of 0.48, both utilizing a Na_2O content of 4.0 wt % (Bernal et al., 2013a). When both samples have a similar carbonation depth (12–15 mm), the AAS concrete (~66 wt% aggregate) showed a more serious decalcification (a decrease of Ca/Si ratio from ~0.7 to ~0.25) compared to the Ref 0.45. It suggests that the small content of aggregate used in this study for the purpose of waste immobilization might not significantly impact the carbonation resistance of AAS. Furthermore, dealumination was also evident in the C-A-S-H gel during carbonation due to the lack of Ca^{2+} (the result of decalcification) for charging AlO_4^- in the gel. This is supported by the observed slight reduction in Al/Si ratios from 0.44 to 0.41 for AAS 0.35, from 0.48 to

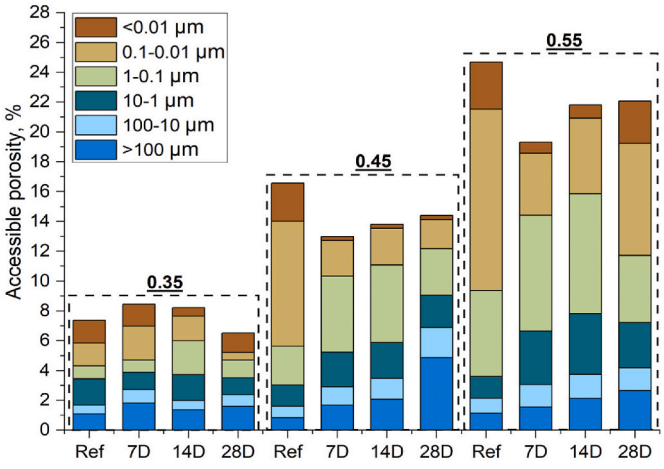

Fig. 8. Accessible porosity and pore size proportion of the AASs during carbonation (calculated from the pore volume fractions assessed by MIP and the bulk density of the corresponding samples).

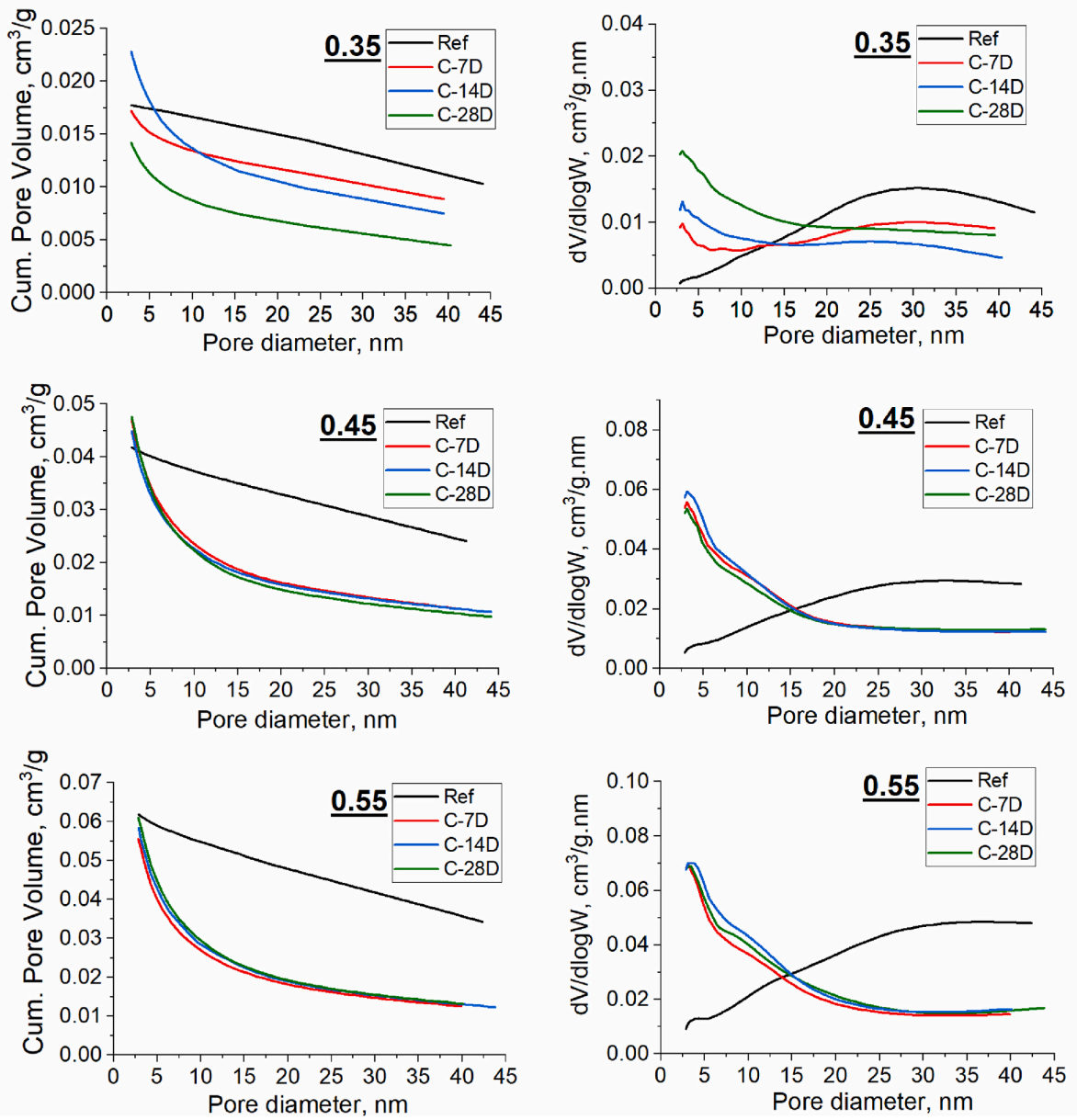

Fig. 9. Cumulative pore volume (left) and pore size distribution (right) of the AASs before (Ref) and after carbonation (7 days: C-7D, 14 days: C-14D, 28 days: C-28D), assessed by N_2 adsorption.

0.46 for AAS 0.45, and from 0.46 to 0.41 for AAS 0.55. The dealumination is also indicated by their NMR results (Nguyen et al., 2022).

4.3. Effect of carbonation on pore structure

4.3.1. Carbonation induced microstructural changes quantified by MIP

Fig. 7 illustrates the cumulative pore volume and pore size distribution (PSD) in the pore size range between 0.007 and 450 μm obtained by MIP for the AASs before and after carbonation. To visualize the microstructural changes over different pore size ranges, the total MIP accessible porosities and the porosity proportions vs corresponding pore size ranges are summarized and shown in Fig. 8. For Ref samples, porosity significantly increased with increasing in the w/b ratio, presenting by a factor of over two and three for Ref 0.45 and Ref 0.55 compared to the Ref 0.35, respectively. Also, previous studies has consistently highlighted the sensitivity of AAS's pore structure to variations in the w/b ratio. For example, the total porosity increased from 31.1% to 40.8% when the w/b ratio raised from 0.35 to 0.45 (Li et al., 2019; Chen and Brouwers, 2006). The main critical pore size of Ref 0.35 situated between 0.01 and 0.04 μm, while the matrices of Ref 0.45 and Ref 0.55 displayed a broader distribution across a range of pore sizes from 0.01 μm to approximately 0.1 μm (Fig. 7-right). The difference among the pore structures can be attributed to the w/b ratio effect on the dissolution/activation process. By using the same Na_2O content (~4 wt % GGBFS) for all Ref samples (Table 2), the case with a higher water content (higher w/b ratio) has a lower alkaline concentration, and thereby potentially leading a lower polymerization degree.

After 28 days of carbonation (C-28D), the total porosity of all samples decreased, potentially attributed to the presence of carbonate precipitates, as indicated by TG analysis. As expected, the AAS with the lowest w/b ratio of 0.35 exhibited the least alteration in its pore structure during carbonation, with an approximately 1% reduction of total porosity. Its PSD (Fig. 7-right) primarily situated at the pore size range smaller than 0.04 μm over the carbonation durations. These could be due to the small amount of formed crystalline $CaCO_3$ (Table 3), which was not enough to lead a significant microstructural change. In contrast,

Table 4
Pore structure of AAS assessed by N_2 adsorption.

w/b ratio	Sample ID	BJH adsorption average pore diameter (4 V/A) (nm)	BET surface area (m^2/g)	Porosity (2–45 nm), BJH (%)
0.35	Ref 0.35	22.71	3.25	3.40
	C-7D 0.35	12.66	8.41	3.22
	C-14D 0.35	8.58	14.11	4.26
	C-28D 0.35	8.81	10.32	2.65
0.45	Ref 0.45	18.69	7.59	7.02
	C-7D 0.45	7.27	41.43	8.43
	C-14D 0.45	7.33	35.03	8.17
	C-28D 0.45	6.96	44.50	8.71
0.55	Ref 0.55	18.09	12.65	10.07
	C-7D 0.55	7.06	52.63	9.45
	C-14D 0.55	7.17	49.07	10.04
	C-28D 0.55	7.12	53.40	10.63

the pore structure of the AAS 0.45 and AAS 0.55 tended to be more heterogeneous during carbonation. Two main critical pore sizes were distinguishably observed in these carbonated samples, especially in C-7D and C-14D: the first PSD consisted of mesopores, typically around 0.015 μm, while the second one comprised small-macropores, approximately 0.14 μm. Previous studies (Puertas et al., 2006; Nedeljković et al., 2018b; Park et al., 2018) noted the coarsen pore structure of different AASs induced by carbonation, which was assigned to changes in the gel structure due to decalcification and formation of microcracks. In this study, small peaks between 4 μm and 9 μm presented in the carbonated samples (Fig. 7-right), possibly implying the formation of microcracks. Crack formation was also observed in the carbonated AAS paste by Nedeljković et al. (Nedeljković et al., 2018b). Interestingly, the C-28D 0.55 demonstrated its PSD at a smaller pore size range than its corresponding C-7D and C-14D. This might be attributed to the more crystalline carbonate products formed after 28 days of the carbonation, thereby refining the pore structure. This trend was also reported by Puertas et al. (2006) as the higher mesopore fraction of a 8-month carbonated AAS compared to that of a 4-months carbonated sample. Furthermore, the porosity fractions at different pore size ranges (Fig. 8) also showed that the porosity of Ref samples mainly come from the gel and meso scales (<0.1 μm), whereas the mesopores and small macropores (0.01–1 μm) remarkably occupied the porosity of carbonated samples.

4.3.2. Carbonation induced nanostructural changes observed by N_2 adsorption

The information derived from MIP for pore sizes below 0.01 μm might be not completely reliable. The volume of such small pore size is potentially overestimated due to the high pressure applied during the MIP measurements, which can cause structural damage (Feldman, 1984; Zuo and Ye, 2018). Hence, it would be more appropriate to evaluate the pore structure at the small pore size scale using N_2 adsorption. Fig. 9 shows the pore volume and PSD between 2 and 50 nm of the AASs before and after carbonation durations. In agreement with MIP results, the porosity of Ref samples in the (2–50 nm) range significantly increased over increasing the w/b ratio, i.e., an approximately twice and threefold higher porosity when increasing the w/b ratio from 0.35 to 0.45 and 0.55, respectively. A very small peak at approximately 3.5 nm was observed in the Ref 0.45 and Ref 0.55 (Fig. 9-right). This pore size corresponds to the intrinsic pores between the C-A-S-H gel clusters in the matrix (Zhang et al., 2019). A larger pore size range (10–50 nm) exhibited a broad distribution centered at around 23 nm for Ref 0.35 and a range spanning from 10 to 40 nm for Ref 0.45 and Ref 0.55. The larger pores were assigned to the space between C-A-S-H gel units (Zhang et al., 2019).

After carbonation durations, insignificant change in the total pore volume was evident (Fig. 9-right and Table 4). However, the PSD curves (Fig. 9-right) show only an intensive peak around 4 nm and a limited spanning to the larger pore size range, suggesting a reduction in the space between gel units after carbonation. This was attributed to the filling of crystalline carbonate products in the space. Notably, the total porosity and PSD of AAS 0.45 and 0.55 at the nano-meso scale (2–50 nm) were relatively stable after 7 days of the carbonation, whereas that of AAS 0.35 seemed to change gradually over the carbonation durations. This is consistent with the lowest carbonation rate of the AAS 0.35, as indicated by its carbonation depth and TG results.

Alteration in the porosity and PSD resulted in the changes in the BET specific surface area (SSA) (Table 4). The SSA showed an approximately threefold (AAS 0.35), fivefold (AAS 0.45), and fourfold (AAS 0.55) increase after 7 days of carbonation, and slightly increased at longer exposure durations in most cases. Based on the PSDs (Fig. 9-right) and the average pore diameters (Table 4), it is clear that the pore size of Ref samples were larger than that of the carbonated ones. Therefore, with a similar total pore volume, the carbonated samples with smaller pores should have a higher SSA. An increase in the SSA due to carbonation was also reported for cement paste (Phung et al., 2015b). Furthermore, as indicated in our previous study on the gel structure of these samples by ^{29}Si MAS NMR (Nguyen et al., 2022), the carbonation induced the highly cross-linked (Q^4) C-A-S-H gel, which is similar to the structure of N-A-S-H gel. The SSA of this typical gel is expected to be higher than that of the semi-layer-like structure of C-A-S-H gel.

4.3.3. SEM imaging analysis

At larger pore size range (>10 μm, in particular), the information provided by SEM is expected to compensate for the potential underestimation of larger pores in the results acquired by MIP (Zuo and Ye, 2018). Fig. 10 shows relatively dense matrices of the Ref samples with the appearance of unreacted slag particles and river sand, along with dark regions representing to the pores. A higher pore fraction can be visually observed in the matrix with the higher w/b ratio. Together with the observation from N_2 adsorption and MIP, the w/b ratio is assumed to affect the pore fractions of all pore sizes, ranging from nano, meso to macropores. After 28 days of carbonation, the matrices appeared to have more large pores and micro-cracks potentially caused by carbonation shrinkage (Ye and Radlińska, 2017; Bernal et al., 2014a). Notably, fewer unreacted GGBFS particles were evident in the carbonated matrices, possibly resulted by further dissolution/reaction during the carbonation. The quantitative deconvoluted ^{29}Si MAS NMR also indicated that the remnant slag decreased from approximately 55%–36% after 28 days of carbonation (Nguyen et al., 2022). The remnant GGBFS can be a Ca source for the formation of Ca-contained phases in the carbonated samples. Furthermore, the carbonated images, especially the ones with the w/b ratio of 0.45 and 0.55, showed white ripples. These could be the partially dissolved remnant slag particles or calcium carbonates, or the mixture of both phases. Note that the shape of crystalline $CaCO_3$ formed in carbonated AAS was different from the white round calcite particles observed in carbonated OPC, attributed to difference in the environmental chemistry surrounding the carbonate. As agreed, Li et al. (2017) indicated the hexagonal crystals of almost 0.5 μm $CaCO_3$ in carbonated AAS.

To quantitatively assess the alteration in the pore structure at large pore sizes, the pore segmentation method proposed in (Jacops et al., 2021; Phung et al., 2017) was used to determine the porosity. The results from 10 to 15 segmented SEM images (magnification of 500 ×) was averaged. Fig. 11 shows a consistent decrease in the porosity (determined for pores >1 μm) of all samples after carbonation. This aligns with the overall trend observed by MIP analysis. Interestingly, the most

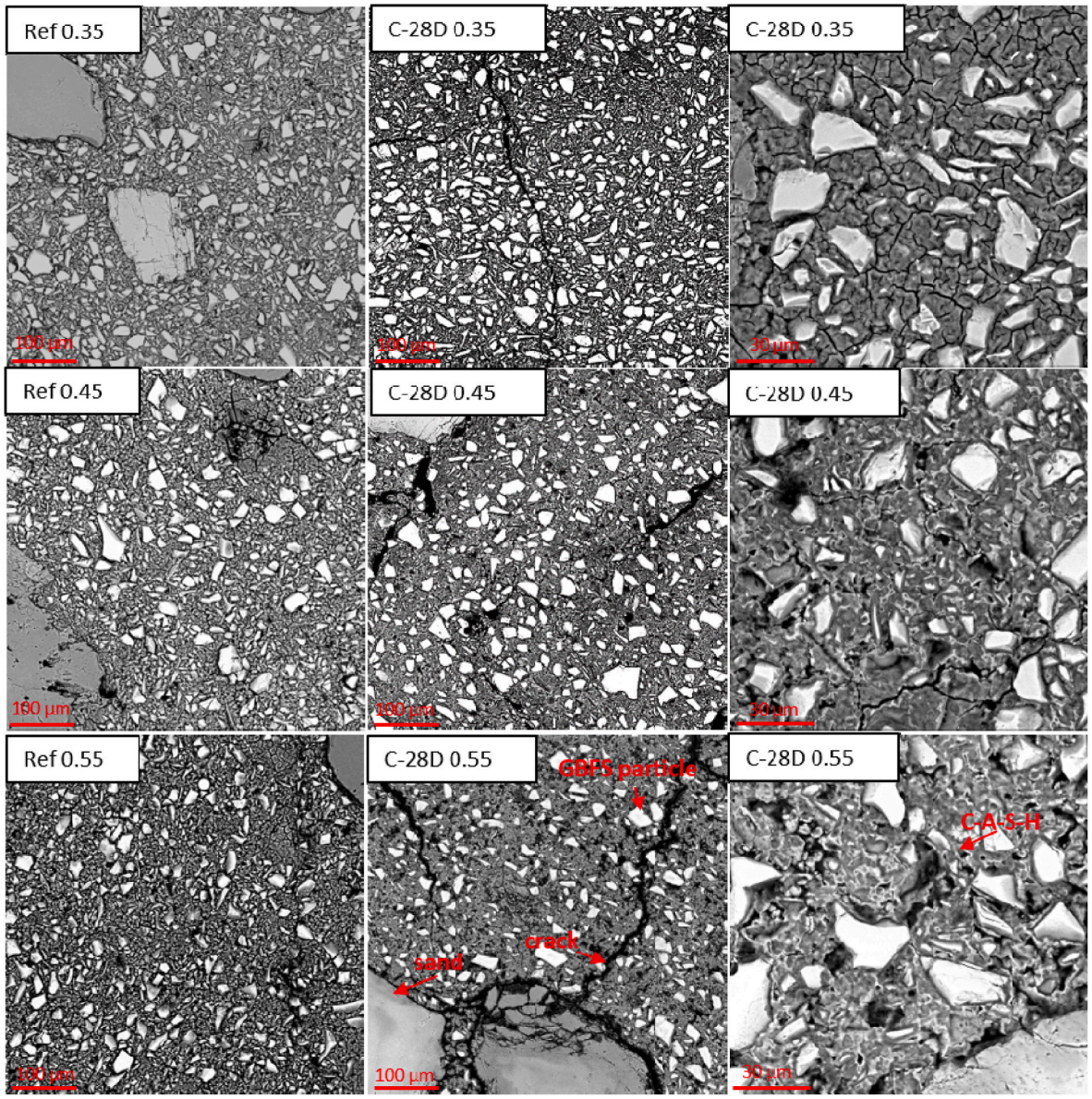

Fig. 10. SEM images of the reference samples (Ref) and 28-day carbonation (C-28D) samples with a magnification of 500 × and 2000 × .

significant change was observed in the porosity of AAS 0.35, which differed from the MIP observation. Note that MIP might underestimate the large pores due to the "ink-bottle" effect (Zuo and Ye, 2018). In contrast, the porosity obtained from the SEM images in this study only counted the pores with a diameter bigger than 1 µm. With the densest matrix of AAS 0.35 (the highest nanopore fraction), the difference between MIP and SEM results of this sample was therefore larger. After carbonation, the PSD (Fig. 11 (bottom row)) of all Ref samples shifted to a smaller pore size range, which was particularly pronounced in the AASs with the higher w/b ratios.

4.4. Residual mechanical strengths and their correlation with microstructure

Alteration in the pore structure of the AASs during the carbonation potentially impacts their mechanical strength. To clarify this, the compressive and flexural strengths of Ref and carbonated samples (C-7D, C-14D, and C-28D) were investigated and shown in Fig. 12. For Ref samples, both compressive and flexural strengths were significantly decreased with increasing the w/b ratio. A decrease of 40% and 55% in the compressive strength and a decrease of 52% and 61% in the flexural strength were observed when the w/b ratio increased from 0.35 to 0.45 and to 0.55, respectively. The higher total porosity and larger PSD resulted in the reduction in the strengths.

During carbonation, the compressive strength of AAS 0.35 showed a slight increase (9%) after 7 days, a further increase (14%) after 14 days, but a slight reduction (5%) after 28 days of carbonation. Due to their limited carbonation depths (Fig. 3), the increase of compressive strength within the 14 first days of exposure might be related to a progressively activating reaction and a minor effect of carbonation. At the longer duration (28 days), the decalcification C-A-S-H gel became more serious, and its weakening effect overwhelmed the strengthening induced by carbonate products. As the result, the compressive strength of C-28D 0.35 slightly decreased compared to that of C-14D 0.35. In contrast to the lowest w/b ratio sample, the compressive strength of the others increased after 7 days of carbonation (e.g., an increase of 32% in C-7D 0.45 and 23% in C-7D 0.55) but reduced after 14 days (a decrease of 8% in C-14D 0.45 and 21% in C-14D 0.55), and further decreased after 28 days of exposure (9% in C-28D 0.45 and 1% in C-28D 0.55). These findings suggest that the decalcification of C-A-S-H gel was more

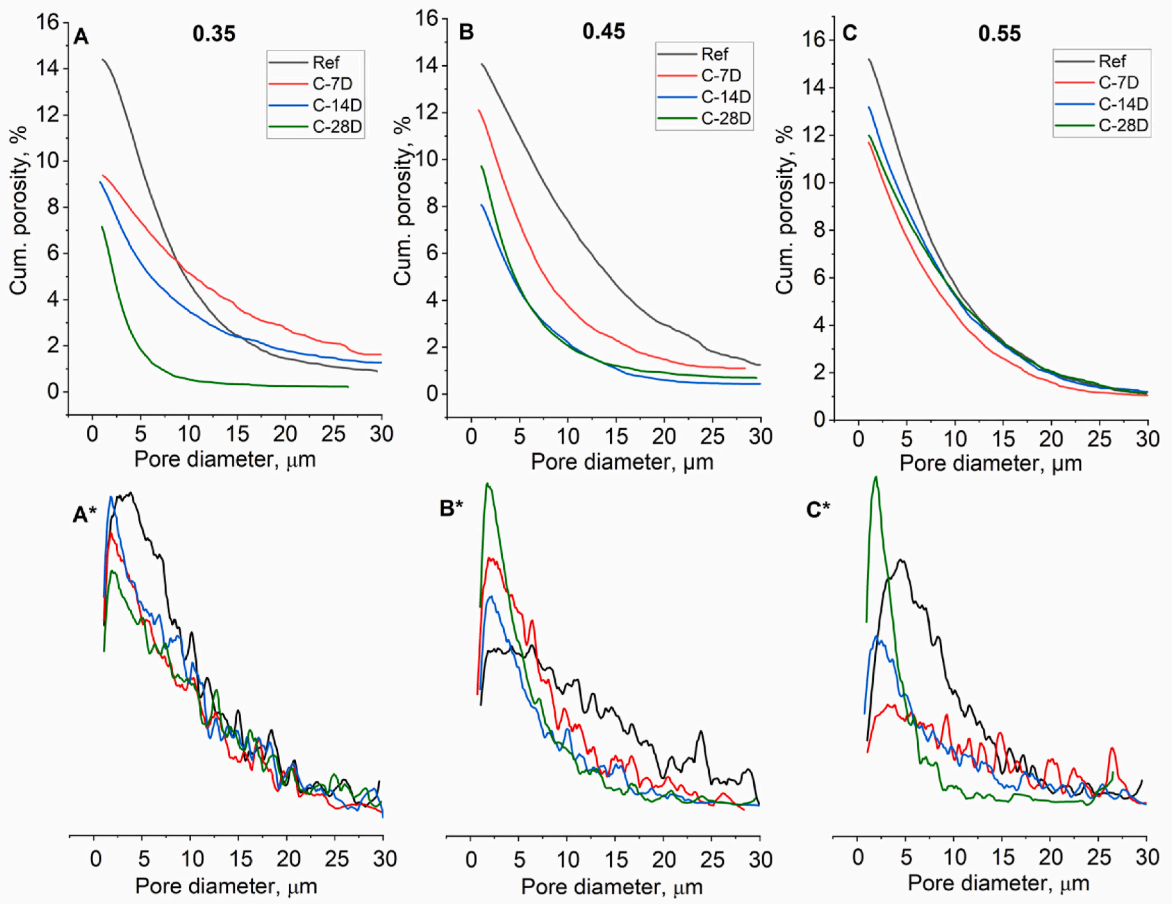

Fig. 11. Cumulative porosity (top) and pore size distribution (bottom) of the reference (Ref) and carbonated samples over carbonation durations (7 days: C-7D, 14 days: C-14D, 28 days: C-28D), assessed by SEM pore segmentation.

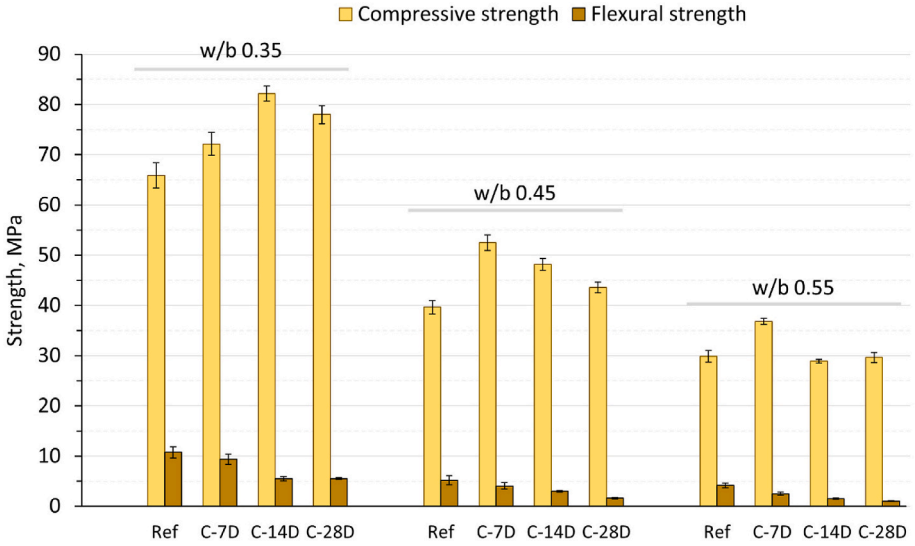

Fig. 12. Compressive and flexural strengths of reference (Ref) and carbonated AASs after 7 days (C-7D), 14 days (C-14D), and 28 days (C-28D) of carbonation.

pronounced in the samples with the higher w/b ratios. As explained, the evolution of compressive strength was associated with the opposite effects caused by the decalcification of C-A-S-H gel (weakening effect) and crystalline $CaCO_3$ products (strengthening effect). In addition, the micro-crack formation might negatively influences the compressive strength. Reduction in the compressive strength of sodium silicate-activated GGBFS during carbonation was also reported (Shi et al., 2018; Puertas et al., 2006).

In contrast to the compressive strength, the flexural strength of the AASs showed a continuous and considerable decrease during the carbonation durations, shown in Fig. 12. After 28 days of carbonation, the flexural strength of AASs with the w/b ratio of 0.35, 0.45, and 0.55

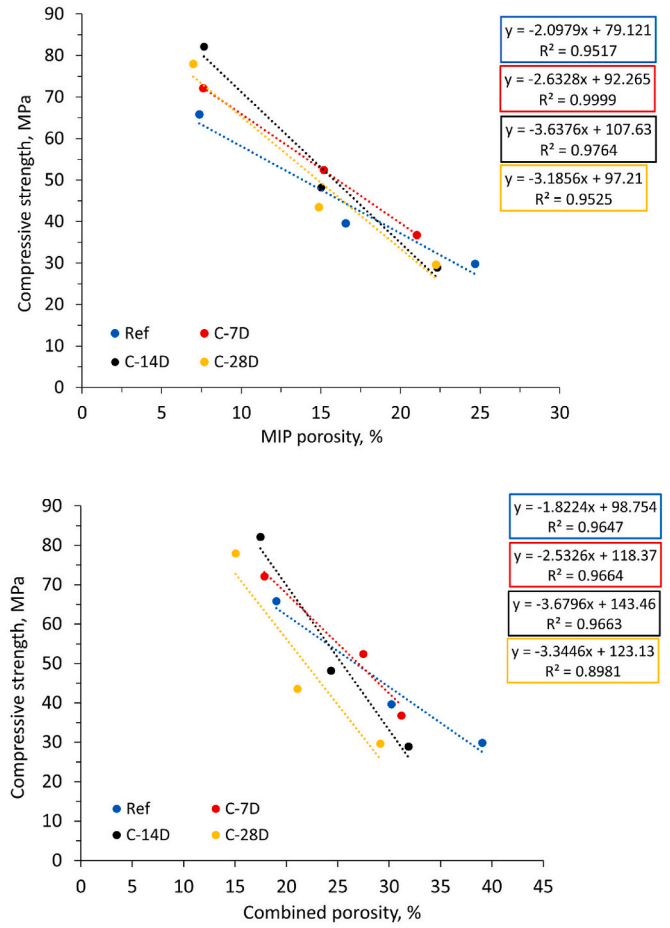

Fig. 13. Correlation between compressive strength and porosity (determined by MIP – top and by a combination – bottom) of the reference (Ref) and carbonated AASs (C-7D, C-14D, C-28D) – The dashed lines represent their linear trends.

showed a reduction of 49%, 69%, and 76%, respectively. The decrease was potentially driven by cracking caused by drying shrinkage and volume expansion under (re)crystallization stress during carbonation, as mentioned above, (Ye and Radlińska, 2017) rather than by the evolution in porosity. Cracking is believed to impact the flexural strength rather than the compressive strength (Qu et al., 2020). The SEM images also showed the appearance of micro-cracks in the carbonated samples, even cracks were visually observed on the surface of the carbonated samples with the w/b ratio of 0.45 and 0.55 (Appendix).

To deeply investigate the relationship between the compressive strength and porosity of the AASs during the carbonation, their evolutions are illustrated together in Fig. 13. It is worth noting that the compressive strengths of the carbonated samples were residual strengths (composite strengths) because these samples were not fully carbonated (evidenced by Fig. 3). Therefore, the porosities of these samples were calculated, taking into account the porosities of both carbonated and uncarbonated parts. The porosity of the carbonated part (colorless part shown in Fig. 2) was assigned to the values determined by the different techniques as discussed above; while the porosity of uncarbonated part (purple core) could be considered to that of the corresponding reference sample. This kind of the estimation approach was also used to interpret the partially degraded cement (Phung et al., 2016; Benbow et al., 2005). The porosities of the carbonated (composite) samples (Fig. 13), are therefore the average values obtained from that calculation. Herein, the average porosity calculated from MIP (called as MIP porosity) is shown. To diminish the less reliability of MIP data at the small-nanopore and large pore range, an approach to combine the porosity information from all three techniques (N_2-ads, MIP, and SEM) was applied (Phung et al., 2017) to obtain the "combined porosity" (Fig. 13). It was incorporated from the porosity in the pore size ranges of 2–10 nm (from N_2 adsorption), 10 nm-1 μm (from MIP), and 1–30 μm (from SEM).

Fig. 13 shows a linear increase of the compressive strength with increasing the average porosity (high R^2 values), occurring in both Ref and carbonated AASs. A good correlation between porosity and compressive strength was also observed for the activated GGBFS/slag blend binders (Cercel et al., 2021; Shariati et al., 2021). However, a relationship between these parameters for carbonated AAMs has not reported so far. This study contributed to address the remaining questionable aspect. In general, regardless of the techniques used to assess porosity, a decrease in the total porosity resulted in an increase in the compressive strength. However, alteration in the compressive strength of the AASs became more sensitive with changes in the total porosity after carbonation, evidenced by the higher slopes of the trend lines for C-7D, C-14D, and C-28D than that for Ref samples (Fig. 13). This implies changes in the microstructural nature of the AAS during carbonation, consistent with the observation in cementitious materials (Phung et al., 2016). The formation of crystalline $CaCO_3$ might overwhelm the adverse impact of the C-A-S-H decalcification. Consequently, despite experiencing an equivalent reduction in the porosity, the carbonated samples exhibited a greater enhancement in the strength compared to their Ref counterparts. In most cases, the longer the carbonation durations, the more sensitive the compressive strength with porosity. Furthermore, the compressive strength over the carbonation durations was more sensitive to the combined porosity rather than to the MIP porosity.

5. Conclusions

Evolution of microstructure and mechanical strength of AAS mortars with different w/b ratios, designed for potential radioactive waste immobilization, upon accelerated carbonation (1% CO_2, 20 °C, and 60% RH) were comprehensively investigated in this study. The conclusions can be drawn as follows:

- An increase in the w/b ratio within the investigated range from 0.35 to 0.55 significantly accelerated the carbonation rate (~ fivefold increase) of the AAS mortars, CO_2 uptake, and decalcification of C-A-S-H. The higher w/b ratios preferably induced the formation of crystalline carbonates (vaterite), whereas more amorphous and less crystalline carbonates formed in the AASs with the lower w/b ratios. The Ca/Si ratio of C-A-S-H decreased by up to 40% after 28 days of carbonation.
- The total porosity of the AASs increased more than twice and threefold when the w/b ratio increased from 0.35 to 0.45 and 0.55, respectively. Upon carbonation, the total porosity generally decreased but tended to slightly increase along the carbonation durations due to the PSD expansion to the larger pore size ranging from 0.1 μm to 1 μm. The volume of nano-mesopores (2–45 nm) was mostly maintained or slightly increased; the volume of mesopores (0.1–1 μm) increased, whereas the volume of larger pores (>1 μm) decreased.
- In agreement with the evolution in pore structure, the compressive strength of AASs increased within 7 days (14 days for AAS 0.35) of carbonation but tended to decrease during longer exposure. A combination between the strengthening effect induced by the formation of crystalline carbonates and the weakening impact of the C-A-S-H decalcification controlled the evolution of the compressive strength. In contrast to the compressive strength, the flexural strength of AASs notably decreased during carbonation periods, with reductions of around 49%, 69%, and 76% in AASs with w/b ratios of 0.35, 0.45, and 0.55 after 28 days of carbonation, respectively. This was primarily due to the influence of cracking.
- The compressive strength of both reference and carbonated AASs increased linearly with a decrease in the total porosity (assessed

either by MIP or by a combination of N_2 adsorption, MIP, and SEM techniques). Interestingly, carbonation induced a more sensitivity of the compressive strength on changes in the total porosity, confirming an alteration in other microstructural characteristics of AAS besides porosity during carbonation.

In general, the AAS mortars designed for liquid radioactive waste immobilization are susceptible to carbonation. However, their performances were not worse than conventional AAS mortars. The pore size distribution mostly fell in the range between 0.01 μm and 1 μm, regardless uncarbonated and carbonated AASs, might offer an appropriate AAS matrix for the deposition of liquid waste. Moreover, the defined correlation between the compressive strength and total porosity of AASs during carbonation can benefit to the design of materials with an expected strength evolution during their service life.

CRediT authorship contribution statement

Thi Nhan Nguyen: Writing – review & editing, Writing – original draft, Visualization, Methodology, Investigation, Formal analysis, Data curation, Conceptualization. **Quoc Tri Phung:** Writing – review & editing, Visualization, Supervision, Resources, Project administration, Methodology, Investigation, Funding acquisition, Data curation, Conceptualization. **Lander Frederickx:** Writing – review & editing, Visualization, Methodology, Investigation, Conceptualization. **Diederik Jacques:** Writing – review & editing, Supervision, Investigation. **Alexandre Dauzeres:** Writing – review & editing, Visualization, Supervision, Investigation. **Jan Elsen:** Writing – review & editing, Supervision, Investigation. **Yiannis Pontikes:** Writing – review & editing, Supervision, Investigation, Conceptualization.

Declaration of competing interest

The authors declare that they have no known competing financial interests or personal relationships that could have appeared to influence the work reported in this paper.

Data availability

Data will be made available on request.

Acknowledgement

This work received funding (in part) from the Belgian Energy Transition Fund (ASOF project), IRSN (France), and the European Union's Horizon 2020 Research and Innovation Programme for Nuclear Fission and Radiation Protection Research (Call NFRP-2019-2020) under grant agreement No. 945098 (PREDIS).

Appendix

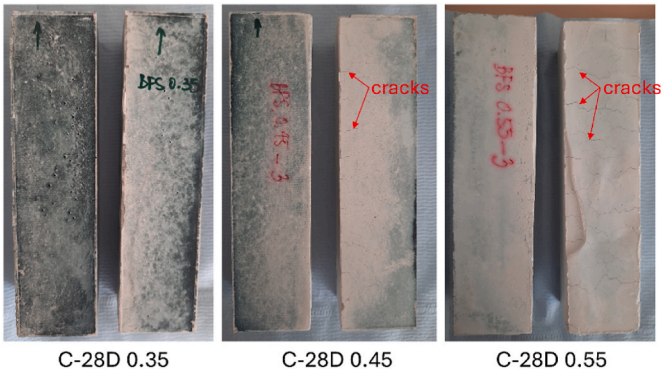

Fig. 14. Images of AAS prisms after 28 days of carbonation

References

Abdalqader, A., Jin, F., Al-Tabbaa, A., 2019. Performance of magnesia-modified sodium carbonate-activated slag/fly ash concrete. Cement Concr. Compos. 103, 160–174.
Bakharev, T., Sanjayan, J., Cheng, Y.-B., 2001a. Resistance of alkali-activated slag concrete to carbonation. Cement Concr. Res. 31 (9), 1277–1283.
Bakharev, T., Sanjayan, J., Cheng, Y.-B., 2001b. Resistance of alkali-activated slag concrete to carbonation. Cement Concr. Res. 31 (9), 1277–1283.
Barrett, E., Joyner, L., Halenda, P., 1951. Pore size distribution for porous materials. J. Am. Chem. Soc. 73, 373–380.
Ben Haha, M., Le Saout, G., Winnefeld, F., Lothenbach, B., 2011. Influence of activator type on hydration kinetics, hydrate assemblage and microstructural development of alkali activated blast-furnace slags. Cement Concr. Res. 41 (3), 301–310.
Benbow, S., Watson, C., Savage, D., 2005. Investigating Conceptual Models for Physical Property Couplings in Solid Solution Models of Cement. Swedish Nuclear Power Inspectorate.
Bernal, S.A., 2015. Effect of the activator dose on the compressive strength and accelerated carbonation resistance of alkali silicate-activated slag/metakaolin blended materials. Construct. Build. Mater. 98, 217–226.
Bernal, S.A., de Gutiérrez, R.M., Pedraza, A.L., Provis, J.L., Rodriguez, E.D., Delvasto, S., 2011. Effect of binder content on the performance of alkali-activated slag concretes. Cement Concr. Res. 41 (1), 1–8.
Bernal, S.A., Provis, J.L., Brice, D.G., Kilcullen, A., Duxson, P., van Deventer, J.S.J., 2012. Accelerated carbonation testing of alkali-activated binders significantly underestimates service life: the role of pore solution chemistry. Cement Concr. Res. 42 (10), 1317–1326.
Bernal, S.A., San Nicolas, R., Provis, J.L., Mejía de Gutiérrez, R., van Deventer, J.S.J., 2013a. Natural carbonation of aged alkali-activated slag concretes. Mater. Struct. 47 (4), 693–707.
Bernal, S.A., Provis, J.L., Walkley, B., San Nicolas, R., Gehman, J.D., Brice, D.G., Kilcullen, A.R., Duxson, P., van Deventer, J.S.J., 2013b. Gel nanostructure in alkali-activated binders based on slag and fly ash, and effects of accelerated carbonation. Cement Concr. Res. 53, 127–144.
Bernal, S.A., San Nicolas, R., Myers, R.J., Mejía de Gutiérrez, R., Puertas, F., van Deventer, J.S.J., Provis, J.L., 2014a. MgO content of slag controls phase evolution and structural changes induced by accelerated carbonation in alkali-activated binders. Cement Concr. Res. 57, 33–43.
Bernal, S.A., San Nicolas, R., Myers, R.J., de Gutiérrez, R.M., Puertas, F., van Deventer, J. S., Provis, J.L., 2014b. MgO content of slag controls phase evolution and structural changes induced by accelerated carbonation in alkali-activated binders. Cement Concr. Res. 57, 33–43.
Bernal, S.A., Provis, J.L., De Gutiérrez, R.M., van Deventer, J.S., 2015a. Accelerated carbonation testing of alkali-activated slag/metakaolin blended concretes: effect of exposure conditions. Mater. Struct. 48 (3), 653–669.
Bernal, S., San Nicolas, R., Van Deventer, J., Provis, J., 2015b. Water content modifies the structural development of sodium metasilicate-activated slag binders. J. Latin-American Assoc. Quali. Contr. Patholo. Recove. Construc. 15 (1), 30–41.

Cadore, D.E., Angulski da Luz, C., Farias de Medeiros, M.H., 2019. An investigation of the carbonation of alkaline activated cement made from blast furnace slag generated by charcoal. Construct. Build. Mater. 226, 117–125.
Cantarel, V., Nouaille, F., Rooses, A., Lambertin, D., Poulesquen, A., Frizon, F., 2015. Solidification/stabilisation of liquid oil waste in metakaolin-based geopolymer. J. Nucl. Mater. 464, 16–19.
Cantarel, V., Lambertin, D., Poulesquen, A., Leroux, F., Renaudin, G., Frizon, F., 2018. Geopolymer assembly by emulsion templating: emulsion stability and hardening mechanisms. Ceram. Int. 44 (9), 10558–10568.
Cercel, J., Adesina, A., Das, S., 2021. Performance of eco-friendly mortars made with alkali-activated slag and glass powder as a binder. Construct. Build. Mater. 270.
Chen, W., Brouwers, H.J.H., 2006. The hydration of slag, part 1: reaction models for alkali-activated slag. J. Mater. Sci. 42 (2), 428–443.
Chen, J.J., Thomas, J.J., Jennings, H.M., 2006. Decalcification shrinkage of cement paste. Cement Concr. Res. 36 (5), 801–809.
Choi, J.-I., Lee, Y., Kim, Y.Y., Lee, B.Y., 2017. Image-processing technique to detect carbonation regions of concrete sprayed with a phenolphthalein solution. Construct. Build. Mater. 154, 451–461.
Feldman, R., 1984. Pore structure damage in blended cements caused by mercury intrusion. J. Am. Ceram. Soc. 67 (1), 30–33.
Frederickx, L., Nguyen, T.N., Phung, Q.T., 2022. Strength and microstructure characteristics of metakaolin-based geopolymer mortars with high water-to-binder ratios. Sustainability 14 (6), 3141.
Hertel, T., Pontikes, Y., 2020. Geopolymers, inorganic polymers, alkali-activated materials and hybrid binders from bauxite residue (red mud)–Putting things in perspective. J. Clean. Prod. 258, 120610.
Jacops, E., Phung, Q.T., Frederickx, L., Levasseur, S., 2021. Diffusive transport of dissolved gases in potential concretes for nuclear waste disposal. Sustainability 13 (18), 10007.
Jin, F., Gu, K., Al-Tabbaa, A., 2014. Strength and drying shrinkage of reactive MgO modified alkali-activated slag paste. Construct. Build. Mater. 51, 395–404.
Lecomte, I., Henrist, C., Liégeois, M., Maseri, F., Rulmont, A., Cloots, R., 2006. (Micro)-structural comparison between geopolymers, alkali-activated slag cement and Portland cement. J. Eur. Ceram. Soc. 26 (16), 3789–3797.
Lee, N.K., Koh, K.T., Kim, M.O., An, G.H., Ryu, G.S., 2017. Physicochemical changes caused by reactive MgO in alkali-activated fly ash/slag blends under accelerated carbonation. Ceram. Int. 43 (15), 12490–12496.
Li, N., Farzadnia, N., Shi, C., 2017. Microstructural changes in alkali-activated slag mortars induced by accelerated carbonation. Cement Concr. Res. 100, 214–226.
Li, Q., Yang, K., Yang, C., 2019. An alternative admixture to reduce sorptivity of alkali-activated slag cement by optimising pore structure and introducing hydrophobic film. Cement Concr. Compos. 95, 183–192.
McCaslin, E.R., White, C.E., 2021. A parametric study of accelerated carbonation in alkali-activated slag. Cement Concr. Res. 145.
Mei, K., Gu, T., Zheng, Y., Zhang, L., Zhao, F., Gong, P., Huang, S., Zhang, C., Cheng, X., 2021. Effectiveness and microstructure change of alkali-activated materials during accelerated carbonation curing. Construct. Build. Mater. 274.
Myers, R.J., L'Hôpital, E., Provis, J.L., Lothenbach, B., 2015. Effect of temperature and aluminium on calcium (alumino) silicate hydrate chemistry under equilibrium conditions. Cement Concr. Res. 68, 83–93.
Nedeljković, M., Zuo, Y., Arbi, K., Ye, G., 2018a. Carbonation resistance of alkali-activated slag under natural and accelerated conditions. J. Sustain. Metallu. 4 (1), 33–49.
Nedeljković, M., Šavija, B., Zuo, Y., Luković, M., Ye, G., 2018b. Effect of natural carbonation on the pore structure and elastic modulus of the alkali-activated fly ash and slag pastes. Construct. Build. Mater. 161, 687–704.
Nedeljković, M., Ghiassi, B., van der Laan, S., Li, Z., Ye, G., 2019. Effect of curing conditions on the pore solution and carbonation resistance of alkali-activated fly ash and slag pastes. Cement Concr. Res. 116, 146–158.
Nguyen, T.N., Phung, Q.T., Frederickx, L., Jacques, D., Dauzeres, A., Elsen, J., Pontikes, Y., 2021. Effect of precursors and water to binder ratios on the water permeability of alkali-activated mortars. The 4th International RILEM Conference Microstructure Related Durability of Cementitious Composites. Delft, The Netherlands, p. 10.
Nguyen, T.N., Phung, Q.T., Yu, Z., Frederickx, L., Jacques, D., Sakellariou, D., Dauzeres, A., Elsen, J., Pontikes, Y., 2022. Alteration in molecular structure of alkali activated slag with various water to binder ratios under accelerated carbonation. Sci. Rep. 12 (1), 1–16.
Park, S.M., Jang, J., Lee, H.-K., 2018. Unlocking the role of MgO in the carbonation of alkali-activated slag cement. Inorg. Chem. Front. 5 (7), 1661–1670.
Pavlík, Z., Trník, A., Kulovaná, T., Scheinherrová, L., Rahhal, V., Irassar, E., Černý, R., 2016. DSC and TG analysis of a blended binder based on waste ceramic powder and Portland cement. Int. J. Thermophys. 37 (3).
Phung, Q.T., 2015a. Effects of Carbonation and Calcium Leaching on Microstructure and Transport Properties of Cement Pastes, Department of Structural Engineering. Ghent University, Belgium, p. 249.
Phung, Q.T., 2015b. Effects of Carbonation and Calcium Leaching on Microstructure and Transport Properties of Cement Pastes. Ghent University.
Phung, Q.T., 2015c. Effects of Carbonation and Calcium Leaching on Microstructure and Transport Properties of Cement Pastes. Ghent University.
Phung, Q.T., Maes, N., Jacques, D., 2017. Application of multiple techniques to quantify pore structure of degraded cementitious materials. In: Schutter, G.D., Belie, N.D., Janssens, A., Bossche, N.V.D. (Eds.), XIV DBMC 14th International Conference on Durability of Building Materials and Components. RILEM Publications S.A.R.L., Ghent, Belgium, p. 12.
Phung, Q.T., Maes, N., Jacques, D., Bruneel, E., Van Driessche, I., Ye, G., De Schutter, G., 2015a. Effect of limestone fillers on microstructure and permeability due to carbonation of cement pastes under controlled CO2 pressure conditions. Construct. Build. Mater. 82, 376–390.
Phung, Q.T., Maes, N., Jacques, D., Bruneel, E., Van Driessche, I., Ye, G., De Schutter, G., 2015b. Effect of limestone fillers on microstructure and permeability due to carbonation of cement pastes under controlled CO2 pressure conditions. Construct. Build. Mater. 82 (0), 376–390.
Phung, Q.T., Maes, N., Jacques, D., De Schutter, G., Ye, G., Perko, J., 2016. Modelling the carbonation of cement pastes under a CO2 pressure gradient considering both diffusive and convective transport. Construct. Build. Mater. 114, 333–351.
Predis https://predis-h2020.eu.
Provis, J.L., Palomo, A., Shi, C., 2015. Advances in understanding alkali-activated materials. Cement Concr. Res. 78, 110–125.
Puertas, F., Torres-Carrasco, M., 2014. Use of glass waste as an activator in the preparation of alkali-activated slag. Mechanical strength and paste characterisation. Cement Concr. Res. 57, 95–104.
Puertas, F., Palacios, M., Vázquez, T., 2006. Carbonation process of alkali-activated slag mortars. J. Mater. Sci. 41 (10), 3071–3082.
Puertas, F., González-Fonteboa, B., González-Taboada, I., Alonso, M.M., Torres-Carrasco, M., Rojo, G., Martínez-Abella, F., 2018. Alkali-activated slag concrete: fresh and hardened behaviour. Cement Concr. Compos. 85, 22–31.
Qu, Z.Y., Gauvin, F., Wang, F.Z., Liu, G., Brouwers, H.J.H., 2020. Effect of hydrophobicity on autogenous shrinkage and carbonation of alkali activated slag. Construct. Build. Mater. 264.
Reeb, C., Davy, C.A., Pierlot, C., Bertin, M., Cantarel, V., Lambertin, D., 2022. Emulsification of low viscosity oil in alkali-activated materials. Cement Concr. Res. 162.
Reeb, C., Davy, C.A., De Campos, M., Hosdez, J., Pierlot, C., Albert-Mercier, C., Lambertin, D., 2023. How are alkali-activated materials impacted by incorporating low viscosity organic liquids? Mater. Struct. 56 (1), 11.
Ruan, S., Zhu, W., Yang, E.-H., Weng, Y., Unluer, C., 2020. Improvement of the performance and microstructural development of alkali-activated slag blends. Construct. Build. Mater. 261.
Sahoo, P., Ishihara, S., Yamada, K., Deguchi, K., Ohki, S., Tansho, M., Shimizu, T., Eisaku, N., Sasai, R., Labuta, J., 2014. Rapid exchange between atmospheric CO2 and carbonate anion intercalated within magnesium rich layered double hydroxide. ACS Appl. Mater. Interfaces 6 (20), 18352–18359.
Shah, V., Bishnoi, S., 2018. Carbonation resistance of cements containing supplementary cementitious materials and its relation to various parameters of concrete. Construct. Build. Mater. 178, 219–232.
Shariati, M., Shariati, A., Trung, N.T., Shoaei, P., Ameri, F., Bahrami, N., Zamanabadi, S. N., 2021. Alkali-activated slag (AAS) paste: correlation between durability and microstructural characteristics. Construct. Build. Mater. 267.
C. Shi, D. Roy, P. Krivenko, Alkali-activated Cements and Concretes, CRC press2003.
Shi, Z., Shi, C., Wan, S., Li, N., Zhang, Z., 2018. Effect of alkali dosage and silicate modulus on carbonation of alkali-activated slag mortars. Cement Concr. Res. 113, 55–64.
Song, K.-I., Song, J.-K., Lee, B.Y., Yang, K.-H., 2014. Carbonation characteristics of alkali-activated blast-furnace slag mortar. Adv. Mater. Sci. Eng. 2014, 1–11.
Standard, E., 2009. Methods of Testing Cement-Part 1: Determination of Strength. Turkish Standards Institute, Ankara, Turkey.
Standardization, E.C.f., 2004. Products and Systems for the Protection and Repair of Concrete Structures. Test Methods: Determination of Resistance to Carbonation.
Vogler, N., Lindemann, M., Drabetzki, P., Kühne, H.-C., 2020. Alternative pH-indicators for determination of carbonation depth on cement-based concretes. Cement Concr. Compos. 109.
Xu, Z., Zhang, Z., Huang, J., Yu, K., Zhong, G., Chen, F., Chen, X., Yang, W., Wang, Y., 2022. Effects of temperature, humidity and CO2 concentration on carbonation of cement-based materials: a review. Construct. Build. Mater. 346.
Yamazaki, Y., Kim, J., Kadoya, K., Hama, Y., 2021. Physical and chemical relationships in accelerated carbonation conditions of alkali-activated cement based on type of binder and alkali activator. Polymers 13 (4).
Yang, T., Gao, X., Zhang, Q., Lv, M., Zhuang, P., Chen, D., 2023. Accelerated carbonation of one-part sodium carbonate-activated slag cements modified by calcined dolomite. Construct. Build. Mater. 375.
Ye, H., Radlińska, A., 2017. Carbonation-induced volume change in alkali-activated slag. Construct. Build. Mater. 144, 635–644.
Ye, H., Cartwright, C., Rajabipour, F., Radlińska, A., 2017. Understanding the drying shrinkage performance of alkali-activated slag mortars. Cement Concr. Compos. 76, 13–24.
Ye, H., Cai, R., Tian, Z., 2020. Natural carbonation-induced phase and molecular evolution of alkali-activated slag: effect of activator composition and curing temperature. Construct. Build. Mater. 248.
Zhang, Z., Zhu, Y., Zhu, H., Zhang, Y., Provis, J.L., Wang, H., 2019. Effect of drying procedures on pore structure and phase evolution of alkali-activated cements. Cement Concr. Compos. 96, 194–203.
Zhang, J., Shi, C., Zhang, Z., 2021. Effect of Na2O concentration and water/binder ratio on carbonation of alkali-activated slag/fly ash cements. Construct. Build. Mater. 269.
Zuo, Y., Ye, G., 2018. Pore structure characterization of sodium hydroxide activated slag using mercury intrusion porosimetry, nitrogen adsorption, and image analysis. Materials 11 (6).